Modeling and Control of Combustion Dynamics in Lean-Premixed Swirl-Stabilized Combustors

Ying Huang and Vigor Yang
The Pennsylvania State University, University Park, PA 16802, *USA*

Abstract

A unified investigation, comprising both numerical simulation and analytical modeling, has been conducted to study the combustion dynamics in lean-premixed (LPM) swirl-stabilized combustors. The numerical analysis treats the conservation equations in three dimensions and takes into account finite-rate chemical reactions and variable thermophysical properties. Turbulence closure is achieved by means of a large-eddy simulation technique. Premixed turbulent combustion is treated using a level-set flamelet library approach. Emphasis is placed on the key mechanisms and operation parameters responsible for driving combustion oscillations. A companion reduced-order model based on a generalized wave equation is established to facilitate data analysis and to help transfer the LES results to a form that can be effectively used to predict the combustion stability characteristics of a full-scale gas turbine engine. The analytical model then serves as backbone for devising control techniques to modulate combustion processes.

1. Introduction

Gas-turbine engines have traditionally used diffusion-flame combustors because of their reliable performance and reasonable stability characteristics. Unfortunately, this type of combustor produces unacceptable high levels of thermal NO_x. The increasingly strict regulation of pollutant emissions has recently urged engine manufactures to turn to the concept of lean premixed (LPM) combustion as an effective means to fulfill the regulatory requirements. [1,2] With LPM combustion, the fuel and air are premixed upstream of the combustor to avoid stoichiometric regions. The combustion zone is operated with excess air to reduce the flame temperature, and consequently thermal NO_x is virtually eliminated. However, unsteady flow oscillations, usually referred to as combustion instability or dynamics, have often emerged as a common problem and hindered the development of LPM combustors. These oscillations in the flowfield may reach sufficient amplitudes to interfere with engine operation. In extreme cases, the ensuing structural vibration and excessive heat transfer to the chamber lead to failure of the system.

Combustion instabilities may be regarded as the unsteady motions in a dynamical system capable of sustaining large oscillations over a broad range of frequencies. Because fluctuations arise from causes internal to the system, they are true instabilities and an external observer perceives the result as the dynamical behavior of a self-excited system. The prevalence of instabilities is primarily attributed to two fundamental reasons [3,4]:

a) combustion chambers are almost entirely closed and the internal processes tending to attenuate unsteady motions are weak; and

b) the energy required to drive unsteady motions represents an exceedingly small fraction of the heat released by combustion.

These underlying issues are present in any combustion chamber, but are especially consequential for gas-turbine engines in which energy intensity is extremely high, typically of the order of 100 $MW/m^3/bar$. In typical instances, less than 0.1% of the energy released in chemical reactions is sufficient to generate pressure fluctuations having peak amplitudes equal to the mean chamber pressure.

The above observations indicate that the possibility of instabilities occurring during the development of new gas-turbine engines must be anticipated and recognized. Stable combustion in the gas turbine combustor may become unstable (oscillatory) due to small changes in operating parameters, geometry configurations, and the manner in which the reactants are introduced. It is well established that the flow and flame dynamics in a combustion chamber can change dramatically as the governing parameters pass through their critical values at which bifurcation points are located. Combustion processes alone may or may not exhibit bifurcation phenomena, but when they take place in the presence of the nonlinear behavior of the chamber dynamics, this sort of characteristic is indeed observed in many combustion devices. [5,6,7] Clearly, a comprehensive understanding of combustion instability is strongly needed to design modifications. Although several mechanisms responsible for driving combustion instabilities, such as hydrodynamic instabilities, equivalence-ratio fluctuations, and flame surface variations, have been proposed and studied, [8,9,10,11,12] many aspects of

---

Corresponding Author: *vigor@psu.edu*

physiochemical processes and operating parameters dictating the initiation and sustaining of instabilities are still unresolved. The situation is further complicated when LPM systems use swirling flow to stabilize the flame with recirculation, which tends to induce vortex breakdown and azimuthal instability, thus exercises profound influences on the combustion dynamics. [13,14] The lack of fundamental information about the flame/flow interaction has seriously jeopardized the establishment of a knowledge-based design methodology to cure the instability problem. Hence, the work herein utilizes contemporary numerical and analytical modeling techniques to address various fundamental issues associated with oscillatory flame dynamics in lean-premixed swirl-stabilized combustors. The analytical model can also serve as backbone for devising control techniques to modulate combustion processes.

Many experimental works [5,6,7,12,15,16,17] have been conducted to investigate the combustion dynamics in LPM combustors. A notable example is the configuration reported by Broda et al. [6] and Seo [17]. The system consists of a single-swirl injector, an axisymmetric chamber, and a choked nozzle, as shown schematically in Fig.1. Natural gas is injected radially from the center body through ten holes immediately downstream of the swirler vanes. The fuel/air mixture is assumed to be well mixed before entering the combustor. A broad range of the equivalence ratio and inlet air temperature was considered systematically. It was found that instabilities take place only if the inlet air temperature is greater that a threshold value T_{in}^* around 660 K and the equivalence ratio falls into the range between 0.5 and 0.7. As the inlet temperature increases and exceeds the threshold value T_{in}^*, the flame bifurcates from a stable state (characterized by a limit cycle with small oscillation) to an unstable state (characterized by a limit cycle with large oscillation). The present study attempts to address this bifurcation phenomenon in flame structure, and to investigate the key mechanisms and operation parameters responsible for initiating and sustaining combustion oscillations.

The remainder of the paper is organized as follows. In section 2, numerical modeling of combustion dynamics in a lean-premixed swirl-stabilized combustor is conducted by means of LES technique. Stable flame evolution, the flame bifurcation phenomenon, and oscillatory flame dynamics under different operation conditions are investigated in detail. In section 3, using LES results a basis, a reduced-order model is developed to determine the stability characteristics of the combustor. Various control strategies are discussed in section 4, and conclusions are presented in Section 5.

2. Numerical Modeling of Combustion Dynamics in a Lean-Premixed Combustor

2.1 Theoretical Formulation and Numerical Method

The basis of the analysis is the LES technique previously developed for investigating LPM combustion instabilities in swirl-stabilized combustors. [8,13,14] The formulation employs the Favre-filtered conservation equations of mass, momentum and energy in three dimensions. The subgrid-scale (SGS) terms are modeled using a compressible-flow version of the Smagorinsky model suggested by Erlebacher et al. [18] The damping function of Van-Driest is used to take into account the flow inhomogeneities near the walls. A level-set flamelet library approach, which has been successfully applied to simulate premixed turbulent combustion, [8] is used here. In this approach, the filtered flame surface evolution is modeled using a level-set G-equation, where G is defined as a distance function outside the flame front. Thermophysical properties are obtained using a presumed probability density function (PDF) along with a laminar flamelet library.

Boundary conditions must be specified to complete the formulation. At the inlet boundary, the mass flow rate and temperature are specified. The pressure is obtained from a one-dimensional approximation to the axial momentum equation, i.e., $\partial p / \partial x = -\rho \partial u / \partial t - \rho u \partial u / \partial x$. The mean axial-velocity distribution follows the one-seventh power law by assuming a fully-developed turbulent pipe flow. The radial and azimuthal velocities are determined from the swirler vane angle. Turbulence properties at the inlet are specified by superimposing broad-band disturbances with an intensity of 15% of the mean quantity onto the mean velocity profiles. In addition, the acoustic response to disturbances arising downstream is modeled by means of an impedance function. [8] At the outlet boundary, the characteristic conditions proposed by Poinsot and Lele [19] are applied, and a time-invariant back pressure is specified as obtained from a simplified one-dimensional momentum equation $\partial p / \partial r = \rho U_\theta^2 / r$ in the radial direction, where U_θ is the mean azimuthal velocity. The pressure at $r = 0$ is fixed as a pre-specified value. Finally, the no-slip adiabatic conditions are enforced along all the solid walls.

The resultant governing equations and boundary conditions are solved numerically by means of a density-based, finite-volume methodology. The spatial discretization employs a second-order, central-differencing method in generalized coordinates. Fourth-order matrix dissipation along with a total-variation-diminishing switch developed by Swanson and Turkel [20] and tested by Oefelein and Yang [21] is included to ensure computational stability and to prevent numerical oscillations in regions with steep gradients. Temporal discretization is obtained using a four-step Runge-Kutta integration scheme. A multi-block domain decomposition technique along with static load balance is used to facilitate the implementation of parallel

computation, with a message-passing interface at the domain boundaries. The theoretical and numerical framework described above has been validated by Huang et al. [8,13,14] and Apte and Yang [21,22] against a wide variety of flow problems in order to establish its credibility and accuracy.

2.2 Physical Model and Grid Resolution

The model combustor shown in Fig. 1 and described in the preceding section is considered in the present study. More detailed information about the experimental facility and results can be found in Ref. 6. The chamber measures 45 *mm* in diameter and 235 *mm* in length. The baseline condition includes an equivalence ratio of 0.573 and a chamber pressure of 0.463 *MPa*. The mass flow rates of natural gas and air are 1.71 and 50.70 *g/s*, respectively. The inlet flow velocity is 86.6 *m/s* and the corresponding Reynolds number based on the inlet flow velocity and height of the inlet annulus is 35000.

According to the experimental observations, the dominant acoustic motion in the axial direction corresponds to the first longitudinal mode. Since there exists an acoustic pressure node at the middle of the chamber, the computational domain includes both a portion of the inlet annulus downstream of the swirler vane and the upstream half of the chamber with a time-invariant back pressure specified at the exit plane. To avoid the numerical singularity along the combustor centerline, a central-square grid system (which consists of a square grid near the centerline and a cylindrical grid in the outer region) is adopted. The entire grid system has 3.44 million points, which are clustered in the shear layers downstream of the dump plane and near the solid walls in order to resolve the steep flow gradients in these regions. The largest grid size (around 0.7 mm) falls in the inertial sub-range of the turbulent kinetic energy spectrum based on the inlet Reynolds number. The computational domain is divided into 72 blocks. All the calculations are conducted on a distributed-memory parallel computer with each block calculated on a single processor.

2.3 Stable Flame Dynamics

Stable flame evolution was first obtained for an inlet mixture temperature of 600 *K* (below the threshold value T_{in}^* for the onset of combustion oscillation) and inlet swirl number of 0.76. The swirl number is defined as the ratio of the axial flux of the tangential momentum to the product of the axial momentum flux and a characteristic radius. The flame bifurcation phenomenon was then investigated by increasing the inlet temperature from 600 to 660 *K*. The mean chamber pressure is 0.463 *MPa*. Figure 2 shows the mean temperature contours and pseudo-streamlines on the $x-r$ plane based on the mean axial and radial velocity components for a stable flame. A central toroidal recirculation zone (CRTZ) is established in the wake of the center body under the effects of the swirling flow. The CTRZ, a form of vortex breakdown, serves as a flame stabilization region, where hot products are mixed with the incoming mixture of air and fuel. In addition, as a result of the sudden increase in combustor area, a corner recirculation zone (CRZ) is formed downstream of the backward-facing step.

The calculated pressure and velocity fields exhibit small-amplitude fluctuations with a dominant harmonic mode at 3214 *Hz,* corresponding to the frequency of the vortex shedding from the center body. Figure 3 presents the flame evolution and vortex shedding process in the upstream region of the chamber over one cycle of oscillation. The pressure and velocity are measured at the middle point of the inlet annulus exit. The phase angle θ is referenced with respect to the acoustic velocity at the interface between the inlet and combustor. The entire process is dictated by the temporal evolution and spatial distribution of the flame front, which moves back and forth under the influences of the vortical motion (indicated by the concentrated streamlines) in the chamber. A new vortex begins to shed from the center body at $\theta = 90^0$, accompanying with a higher local flow velocity. As the vortex moves downstream ($\theta = 180^0 - 270^0$), it distorts the flame front or even produces a separated flame pocket. At the same time, the higher speed mixture pushes the flame downstream. When the vortex moves away from the flame ($\theta = 360^0$) and dissipates into small-scale structures, the flame front propagates upstream (since the higher speed mixture is convected downstream) and interacts with another incoming vortex. During this process, a new vortex appears at the corner of the center body and another cycle repeats.

2.4 Bifurcation of Flame Structure

The inlet temperature has enormous effects on the flame dynamics in the system. On the one hand, when the inlet temperature increases, for a fixed mass flow rate, the flow velocity also increases and pushes the flame downstream. On the other hand, the increased inlet temperature leads to an increase in the flame speed, and consequently causes the flame to propagate upstream. In addition, flashback may occur near the wall due to the small local flow velocity. The combined effects of flow acceleration, flame-speed enhancement, and flashback determine the final form of the flame structure.

In the present study, as the inlet temperature increases from 600 to 660 *K*, flame bifurcation takes place. The flame originally anchored in the center recirculation zone penetrates into the corner recirculation zone and flashes back. Consequently, the flame is stabilized by both the corner- and center-recirculating flows and forms a compact enveloped configuration. The flame flaps dynamically and drives flow oscillations through its influence on unsteady heat release. At the same time, the pressure oscillation increases and reaches another limit cycle with a much larger amplitude. The entire bifurcation process can be divided into three stages: high temperature mixture filling process, flame trapping process, and vortex flashback process, as shown in Fig. 4, where $t = 0\ ms$ denotes the time at which the inlet mixture temperature starts to increase from 600 to 660 *K*.

Figures 4a-4c show the high-temperature mixture filling process. As the inlet mixture temperature increases, the flow speed increases due to the decreased density for a fixed mass flow rate. As a result, the original low-temperature mixture is pushed downstream toward the flame. Although a flashback phenomenon is observed near the wall, the high temperature mixture has not reached the flame front near the wall and the flame speed remains unchanged at this stage.

Figures 4d-4e show the flame trapping process. Once the high temperature mixture reaches the flame front, with the help of the increased flame speed, the near-wall flashback overshadows the flow acceleration effects. Consequently, the flame front penetrates into the corner recirculation zone and is trapped by the local vortical motion.

In the vortex flashback process, as shown in Figs. 4f-4h, the flame propagates upstream under the influence of the vortical motion. A counter-clockwise rotating vortex originally shed from the edge of the backward-facing step approaches the flame front in the corner recirculation zone and then pushes it toward the dump plane. At the same time, a small flame pocket is produced and separated from the main stream. After this vortex is convected downstream and passes through the flame, another vortex approaches and interacts with the flame. This process continues and eventually the fresh reactants in the corner recirculation zone are completely burnt. The flame is stabilized by both the corner- and center-recirculating flows and its overall length is substantially reduced. This situation renders the combustor more prone to instabilities according to the Rayleigh criterion, [23,8] since considerable heat is released within a short distance close to the chamber head-end (i.e., the acoustic anti-node point).

In light of the above observations, we conclude that the flashback phenomenon dictates the flame bifurcation process. Flashback in premixed combustion has been the subject of a number of experimental, analytical, and numerical studies in the past. Its occurrence is usually attributed to two mechanisms. The first involves flame propagation in the boundary layer along a solid wall, where the local velocity diminishes toward the surface. The second mechanism is associated with flow reversal, which is usually caused by vortical motions or acoustic oscillations. Both mechanisms are observed in the present case. A criterion for the occurrence of near-wall flashback was proposed by Lewis and Von Elbe, [24] who state that flashback occurs if the velocity gradient at the wall is less than the ratio of the flame speed and the quenching distance. This criterion, however, is qualitatively correct only for isothermal walls, and is not applicable for adiabatic walls due to the lack of a quenching distance. Another criterion, valid for both adiabatic and isothermal walls, was recently proposed by Kurdyumov et al. [25] Flashback occurs if the Karlovitz number, defined as $\alpha A / S_L^2$, with α being the thermal diffusivity and A the velocity gradient at the wall, is less than a critical value. Although this criterion is formulated for laminar flows, the result can be qualitatively extended to flames in turbulent boundary layers. In the present case, the flame speed increases as the inlet temperature increases. Consequently, the flame is more prone to flashback through the wall boundary layers according to Kurdyumov's criterion. Flashback arising from local flow reversal has also been investigated by many researchers. [26,27] Large vortical structures and turbulent flame speed play important roles in this kind of phenomenon. The latter is essential because it controls the rate of mixture consumption.

For lean-premixed combustion, the laminar flame speed S_L increases with an increase in the equivalence ratio ϕ. Thus, increases in the equivalence ratio and inlet temperature exert similar effects on the flame evolution. However, the chemical reaction rate and heat release are much more sensitive to variations in the equivalence ratio under lean conditions than under stoichiometric conditions. Moreover, near the lean blowout limit, perturbations in the equivalence ratio ϕ can cause periodic extinction of the flame. As a result, the equivalence ratio oscillation under lean conditions is prone to inducing flow oscillation [28] and subsequently increases turbulent velocity fluctuation v'. This suggests that a lean premixed turbulent flame is more susceptible to flashback, since the turbulent flame speed S_T increases not only with the laminar flame speed S_L, but also with turbulent velocity fluctuation v'. [29] The result helps explain why the transition from a stable to an unstable state as described in Ref. 2 only occurs when the equivalence ratio falls in the range between 0.5 and 0.7. Since the flame bifurcation is largely determined by the flashback phenomenon in the corner recirculation zone in the present case, one effective way to avoid its occurrence is to inject cold flow into that region. This procedure suppresses the local flame upstream propagation and consequently leads to a much more stable system.

Once the flame becomes unstable (oscillatory) when the inlet flow temperature exceeds the critical value T_{in}^*, it becomes rather difficult to re-establish stable operation unless the inlet temperature is reduced to a level significantly lower than T_{in}^*. This phenomenon is commonly referred to as hysteresis, and has been experimentally observed by many researchers. [6,17] The occurrence of hysteresis under the current circumstance may be explained as follows. During unstable combustion, the corner recirculation zone is filled with high temperature products and the chamber wall in this region is heated to reach the local flame temperature. To recover stable operation, the cold flow needs not only to extinguish the flame stabilized by the corner recirculating flow through entrainment or flame liftoff, but also to offset the effects of high temperature wall, which tends to increase the local gas temperature and inhibit extinction and near-wall flashback. Consequently, a much lower inlet temperature is required to regain stable operation. Numerical simulation of the hysteresis phenomenon necessitates a refined treatment of flame extinction and wall boundary conditions, a subject for sequent research.

2.5 Oscillatory Flame Dynamics

2.5.1 Mean Flow Structures

Three swirl number, S = 0.44, 0.76 and 1.10, are investigated for unstable flame dynamics. For each swirl number, calculations were performed for about four flow-through times (around 12 ms) after the flowfield had reached its stationary state in order to obtain statistically meaningful data for analyzing the flow dynamics. The mean flow properties are first obtained by taking long-time average of the instantaneous quantities. In spite of significant flow motions in the azimuthal direction, the mean flowfield remains perfectly axisymmetric. Figure 5 shows the streamline patterns and mean temperature fields on the $x-r$ plane. Three distinct recirculation zones are observed in the low-swirl number case with S = 0.44, including a separation wake recirculation zone (WRZ) behind the centerbody, a corner recirculation zone (CRZ) due to the sudden enlargement of the combustor configuration, and a central toroidal recirculation zone (CTRZ) resulting from vortex breakdown. The wake recirculation zone, however, disappears at the high swirl number of S = 1.10. The overall flow development with respect to the inlet swirl number can be described as follows. If there is no swirl, only the wake and corner recirculation zones exist. As the swirl number increases and exceeds a critical value, vortex breakdown takes place and leads to the formation of a central recirculation zone. As the swirl number further increases, the central recirculation zone moves upstream and merges with the wake recirculation zone. Consequently, the corner recirculation zone becomes diminished. Similar results were reported by Chao [30] in his experimental study of the recirculation structure in a co-annular swirl combustor. The mean temperature fields clearly exhibit enveloped flames anchored at the rim of the centerbody and the corner of the backward-facing step. The flame is much more compact for the high swirl number case with S = 1.10, which is due to the enhanced flame speed resulting from the increased turbulence intensity, as we will show later.

Figure 6 shows the radial distributions of the mean velocity components and turbulent kinetic energy at various axial locations for S = 0.44 and 1.10, where $r = 0$ corresponds to the centerline of the chamber. The negative axial velocities in the central and corner regions indicate the existence of recirculation zones. The incoming flows from the inlet annulus spread outward from the chamber centerline under the effect of the centrifugal force, producing positive radial velocities in the main flow passage. The stronger the swirl strength is, the faster the main flow moves toward the wall. As a result, the size of the corner recirculation zone is considerably reduced at the high swirl number of S = 1.10. The mean azimuthal velocity fields suggest that the flow motion in the central region bears a close resemblance to solid-body rotation. The distributions of the turbulent kinetic energy indicate that a high turbulence-intensity region develops downstream of the centerbody and the backward-facing step, where large velocity fluctuations are produced because of the strong turbulent mixing in the shear layers between the incoming flow and the recirculation flows. The evolution of turbulent kinetic energy is governed by the following equation:

$$D(\overline{u_i^2}/2)/Dt = \partial(-\overline{u_j p}/\rho_0 - \overline{u_i^2 u_j}/2 + 2\overline{vu_i e_{ij}})/\partial x_j - \overline{u_i u_j}\partial U_i/\partial x_j - 2\overline{ve_{ij}e_{ij}} \tag{1}$$

where $e_{ij} = (\partial u_i/\partial x_j + \partial u_j/\partial x_i)/2$. The existence of the steep velocity gradient $\partial U_i/\partial x_j$ due to the strong swirling and reverse flow at the high swirl number case facilitates the high production of turbulent kinetic energy, $-\overline{u_i u_j}\partial U_i/\partial x_j$. Consequently, much stronger turbulent kinetic energy is observed for the high swirl number case with S = 1.10.

2.5.2 Instantaneous Flowfield

Vorticity is of concern in the present study because of its dominant influence in determining the flow entrainment in the reaction zone and the subsequent flame evolution. Figure 7 shows snapshots of the vorticity magnitude field on an $x-r$ plane. For the low swirl-number case with S = 0.44, large vortical structures, arising from the shear layers downstream of the dump plane and centerbody, are convected downstream, and

then dissipated into small-scale eddies. The same phenomenon is also observed for the high swirl number case, in which well-organized vortices are shed from the edge of the backward-facing step. The vortex motions downstream of the centerbody, however, become quite disordered, due to the presence of the strong central recirculating flow. In both cases, the vortex shedding frequencies are close to that of the first tangential mode of acoustic wave in the chamber.

Figure 8 shows snapshots of the iso-vorticity surface at $\omega = 75000$ 1/s. The flowfield in the region $r > 2$ *cm* is blanked to provide a clear picture of the vortex structures. For the low swirl number case with S = 0.44, a vortex spiral evolves from the shear layer originating at the backward-facing step, due to the Kelvin-Helmholtz instabilities in both the axial and azimuthal directions. This vortical structure gyrates around the centerline and persists for about several turns before breaking up into small fragments. For the high swirl-number case with S = 1.10, a spiral vortex structure can also be observed. The structure, however, is much more complex, due to the high centrifugal force. It spreads outward rapidly and soon breaks up into small-scale structures.

The evolution of these spiral vortex structures can be regarded as a kind of vortex shedding process with well-defined frequencies, as described previously. One may conjecture [8] that the vortical motions in the shear layers resonate with acoustic oscillations in the chamber. In the present configuration, two shear layers exist downstream of the rear-facing step and the centrebody. The axial momentum thickness, θ_0, of each shear layer is estimated to be around 0.1 *mm* for the low swirl number case based on the calculated mean velocity distribution. For the high swirl number case, the momentum thickness of the lower shear layer (≈ 0.25 *mm*) differs from its upper counterpart (≈ 0.05 *mm*) by a factor of five, due to its stronger swirl strength. A linear stability analysis [31] has been carried out to provide more insight into the shear-layer instability phenomena for annular swirling flows in an open atmosphere. The geometrical parameters were selected to match the current physical model. The effects of momentum thickness, swirl strength, and density and velocity ratios were studied systematically with different azimuthal wave numbers. The predicted most amplified frequencies are different for the two swirl numbers considered herein, mainly due to the disparity of the axial momentum thickness between the two cases. In addition, the predicted values are much higher than the vortex-shedding frequency, which corresponds to the frequency of the first tangential (1T) acoustic mode of motion in the present chamber. This observation indicates that the acoustic oscillation acts as a forced excitation to the system. The shear layers respond to the excitation by locking their shedding frequencies close to the forcing frequency.

2.5.3 Spectral Analysis of Oscillatory Flowfield

The oscillatory flowfield were carefully surveyed to provide direct insight into the driving mechanism for acoustic oscillations. A vast number of probes were employed to register the flow motions in various parts of the chamber. The fast Fourier transform (FFT) technique was used for the spectral analysis. Figure 9 shows the frequency contents of the pressure fluctuations immediately downstream of the dump plane. For *S* = 0.44, the dominant frequencies of 1761, 10367 and 17618 *Hz* correspond to the first longitudinal (1L), first tangential (1T) and second tangential (2T) modes of acoustic motions in the chamber, respectively. The slight deviation from the prediction of the linear acoustic modal analysis results from the uncertainties in specifying the averaged speed of sound and the chamber length. It is worth noting that the experimental measurements' also indicate the existence of the second longitudinal (2L) mode at 3500 *Hz*. This mode, however, was suppressed in the present numerical study since the back pressure at the end of the computational domain was fixed at a pre-specified value, a condition that prohibited the excitation of higher modes of longitudinal oscillations. For *S* = 1.10, the longitudinal wave disappears and the frequencies of the 1T and 2T modes slightly shift to 10,795 and 18,133 *Hz* due to the change in the temperature field. Good agreement in the acoustic mode shape between the calculated and analytical results is obtained for both the 1T and 2T acoustic modes. Although the oscillation frequencies at 22,157 Hz for S = 0.44 and 21,872 Hz for S = 0.11 are close to the first radial (1R) acoustic mode (22,456 Hz), the mode shapes do not match well the analytical result of classical acoustics, thus can not be regarded as the 1R mode. This observation is also confirmed by the POD analysis to be discussed. The inlet swirl number exerts little influence on the acoustic frequencies, but plays a significant role in determining the wave amplitudes. The suppression of low-frequency oscillations in the high swirl number case may be attributed to the enhanced flame stiffness, which reduces the flame sensitivity to imposed disturbances.

2.5.4 Flame Surface and Heat Release Evolution

To understand the mutual coupling between the flame dynamics and flow oscillation, the total heat release and flame surface area were analyzed in the frequency domain. The overall heat release in the chamber can be obtained from

$$\dot{Q} = \rho_u \Delta h_f^0 S_T A \tag{2}$$

where ρ_u is the unburnt gas density, S_T the subgrid turbulent flame speed, and Δh_f^0 the heat of reaction. The total filtered flame surface area, A, can be determined from the following integral

$$A = \int \delta(\widetilde{G}(\mathbf{x})) \left| \nabla \widetilde{G}(\mathbf{x}) \right| d\mathbf{x} \tag{3}$$

where δ is a delta function, which needs to be evaluated numerically. In the level-set flamelet library approach, [8] $\widetilde{G}$ represents a signed distance function with $|\nabla \widetilde{G}| = 1$, and $\widetilde{G} = 0$ corresponds to the filtered flame front. $\delta(\widetilde{G}) = 0$ everywhere except on the lower dimensional interface (i.e., the flame surface). For the sake of simplicity without much compromise in accuracy, a first-order accurate smeared-out approximation of the delta function is usually used [32,33]:

$$\delta(\widetilde{G}) = \begin{cases} [1 + \cos(\pi \widetilde{G} / \varepsilon)] / 2\varepsilon & |\widetilde{G}| < \varepsilon \\ 0 & |\widetilde{G}| > \varepsilon \end{cases} \tag{4}$$

where ε is a tunable parameter that determines the size of the bandwidth of numerical smearing. A typical value of $\varepsilon = 1.5\Delta$ is used, with Δ being the grid width. This method has been widely employed to evaluate the quantities defined on arbitrary interfaces in the areas of multiphase flows, computer vision, and image processing. [32,33]

Figure 10 shows the power spectral densities of the total filtered flame surface-area and heat-release fluctuations. At S = 0.44, a dominant mode exists at 1761 *Hz* in the flame-surface oscillation, which corresponds to the 1L acoustic mode of the combustor. A higher harmonic at 3320 *Hz* is also found, approximately twice the frequency of the 1L mode. Although transverse acoustic motions including the 1T and 2T modes are observed, the flame surface-area oscillations do not exhibit such a high-frequency behavior. At S = 1.10, a small peak at 11712 *Hz* near the 1T acoustic mode is present, but no corresponding 1L mode oscillation is found. The frequency content of the total heat-release fluctuations bears a close resemblance to that of flame surface-area variations. A small spike near the frequency of 20,532 Hz, however, is observed for S = 0.44, which arises from the fluctuations in the subgrid turbulent flame speed S_T. [29] In light of the above observations, one can conclude that low-frequency acoustic perturbations exert a strong influence on the fluctuations of the total flame surface area and heat release. In contrast, high-frequency acoustic oscillations travel through the flame zone without significantly affecting the flame surface area and heat release variations, although they may impose a significant impact on the local flame propagation. The results qualitatively agree well with the prediction from a companion analytical analysis of flame response [44,45]. The calculated mean flame surface area and the root mean square of the fluctuating quantity for the high swirl-number case is much smaller than those of the low swirl-number case. However, owing to the increased turbulence intensity and the ensuing enhancement of the flame speed in the high swirl-number case, the mean heat-release rate and the associated fluctuation are very close in these two cases.

2.5.5 Acoustic and Flame Evolution

Figure 11 presents the temporal evolution of temperature field at T = 1700 K over one cycle of the 1L mode of acoustic oscillation at S = 0.44. The phase angle θ is referenced to the 1L acoustic pressure at the chamber head-end. The entire process is dictated by the cold-flow entrainment into and mixing with hot gases in the vortical structures in the flame zone. Figure 12 shows the time histories of the pressure immediately downstream of the dump plane (top), the total flame surface area (middle) and the rate of heat release (bottom). These signals involve a wide range of frequencies corresponding to turbulent-flow and acoustic oscillations. The extracted 1L oscillations (denoted by the thick black lines) of these quantities are also plotted for clarity. The flame surface-area variation can be elucidated by considering its interaction with the local oscillatory flowfield. It lags behind the pressure oscillation by 76 degrees. During the period from $\theta = -166^o$ (t = 24.09 ms) to 14° (t = 24.38 ms), a relatively lower pressure field exists near the dump plane, facilitating the delivery of the fresh reactants into the chamber. Intensive heat release then occurs after a short fluid-mixing and chemical-induction time. The resultant flow expansion pushes the flame outward, and causes the flame surface area to increase from a trough to a crest. Unburned mixture fragments may be shattered away from the main stream, and generate local hot spots when convected downstream. During the period from $\theta = 14^o$ (t = 24.38 ms) to 194° (t = 24.66 ms), the relatively higher pressure near the dump plane prevents the fresh reactants from traveling downstream into the chamber. The flame zone is thus reduced and becomes a little more compact. The same process then repeats for another cycle of oscillation. Figure 11 also indicates that the heat-release and flame-surface-area fluctuations are nearly in-phase. The former only lags behind the flame surface-area oscillation by 4 degrees. Figure 13 shows the time evolution of the instantaneous Rayleigh index, $p^a \cdot \dot{Q}^a(t)$, over the entire chamber for the 1L mode oscillation. This parameter is positive during most of time, suggesting the excitation and sustenance of the 1L oscillations by the flame. For the high swirl-number case with S = 1.10. No obvious 1L oscillation can be observed, as shown in Fig.14.

Figure 15 presents the temporal evolution of temperature field over one cycle of the 1T mode of acoustic oscillation. As the swirl number increases, the flame anchored by the center recirculating flow may propagate upstream periodically and cause flame flashback. Two mechanisms, as stated previously, have been identified

for the occurrence of flame flashback. In this case, the flashback is closely linked to the strong reverse flow in the center recirculation zone. The swirl strength is so strong that it sometimes causes the center recirculating flow to enter into the inlet annulus. As a consequence, the flame attached to the centerbody travels upstream and flashback occurs.

2.5.6 Vortex and Flame Interaction

Figure16 shows the instantaneous vorticity field at various times within one cycle of the 1T acoustic oscillation for S = 0.76. The thick black line indicates the flame front. Well-organized vortices are shed from the edge of the backward-facing step. The process, however, becomes much more complex in the downstream of the center body due to the existence of a toroidal recirculating flow. New vortices are produced at the tip of backward-facing step at $\theta = 72^0$, and bulge the flame front. They continue to distort the flame or even produce separated flame pockets when traveling downstream. Finally, these vortices move out of the flame region and dissipate into small-scale structures. Another set of vortices appears at $\theta = 360^0$ at the dump plane, and the cycle repeats.

To further examine the above process, the temporal evolution of the vorticity, temperature, and heat-release distributions within one cycle of the 1T mode of acoustic oscillation is plotted for S = 0.76, as shown in Fig. 17. The vortex shedding process is clearly visualized in the evolution of the vortex spiral, which gyrates around the chamber centerline and propagates downstream. The wave-like structure on the flame surface possesses a characteristic frequency corresponding to the 1T acoustic wave. Because the vortex shedding affects the shapes of the flame front, it also changes the heat-release distribution. As a result, the acoustic motion in the chamber is closely coupled with the heat-release fluctuation.

2.5.7 Proper Orthogonal Decomposition Analysis

The combustion dynamics is further explored using the proper orthogonal decomposition (POD) technique. [34,35,36,37,38] The POD analysis takes as input an ensemble of instantaneous realizations or snapshots, which is obtained from physical experiments or numerical simulations, and extracts base functions optimal for the representation of the data. More precisely, if we consider a collection of observations $\mathbf{q}(\mathbf{x}, t_m)$ obtained at M different time steps t_m over a spatial domain of interest Ω, the POD method attempts to determine a set of orthogonal base functions $\boldsymbol{\varphi}^{(n)}(\mathbf{x})$, $n = 1, \ldots, M$, such that the projection of $\mathbf{q}(\mathbf{x}, t_m)$ onto the base functions,

$$\hat{\mathbf{q}}(\mathbf{x}, t_m) = \sum_{n=1}^{M} a^{(n)}(t_m) \boldsymbol{\varphi}^{(n)}(\mathbf{x}) \tag{5}$$

has the smallest error, defined as $<\| \mathbf{q} - \hat{\mathbf{q}} \|^2>$, where $a^{(n)}(t_m)$ is the expansion coefficient. The symbol $<\cdot>$ denotes a time or ensemble average, and $\| \cdot \|$ the norm associated the inner product $(,)$ in the Hilbert space of square integral functions. To compute POD modes, we first need to make an appropriate choice of a vector-valued flow variable $\mathbf{q}(\mathbf{x},t)$ and define a suitable inner product on the configuration space. The POD method using the fluctuating flow-variable vector $\mathbf{q}' = (u', v', w', p')$ and the inner product based on the acoustic potential energy is found to be more effectively in capturing acoustic motions [39], and will be used in the subsequent analysis.

The LES database for the POD analysis contains a total of 200 data sets or snapshots for each swirl number. The spatial domain of concern only includes the upstream portion of the computational domain, and has 2.0 million grid points. The time interval at which the snapshots were sampled was 6.0 μs, compared with the time step of 0.03 μs employed in the numerical simulations. Thus, the total time span was approximately 2.1 and 12.5 times of the 1L and 1T acoustic oscillation periods. The size of each database is around 30 gigabytes and an extensive computer storage space is required for the POD analysis.

Figure 18 shows the energy distributions of the POD modes based on the acoustic pressure fields for two different swirl numbers. In the low swirl-number case with S = 0.44, the first two modes have almost the same energy level (i.e., 31.28 and 29.14%) and collectively capture more than 60% of the total energy of the oscillatory flowfield. A similar observation is made for the high swirl number case with S = 1.10, where the first and second modes represent 37.22% and 34.16% of the total energy, respectively. In both cases, the first 16 modes account for more than 80% of the total energy. The frequency spectra of the time-varying coefficients, $a^{(n)}(t)$, of the first six POD modes are shown in Fig. 19. For the low swirl-number case, the dominant frequencies of 10,435 Hz for the first two modes and 17,889 Hz for the fourth and sixth modes correspond to the 1T and 2T acoustic modes in the chamber, respectively. The same phenomenon occurs with the high swirl number, with the first two modes and modes 3 and 4 associated with the 1T and 2T acoustic mode of oscillations respectively, although the dominant frequencies shift slightly due to the variation in the flowfield. For both swirl numbers, the 1L acoustic mode is not observed. This may be attributed to the relatively short time span of the database compared with the 1L acoustic oscillation period.

Figure 20 shows the spatial distributions of the fluctuating pressure field for the first six POD modes for S = 0.44. The first two modes, shifted from each other by 90 degrees in the azimuthal direction, representing the standing transverse acoustic waves in the chamber. [39] The wave motion is most intensive near the dump plane where heat release takes place, and gradually decays downstream along the length of the chamber. Mode 3 has an axisymmetric distribution, with its strongest oscillations in the shear layer and downstream of the centerbody. Modes 4 and 6 closely resemble the 2T acoustic mode. Their mode shapes differ from each other by 45 degrees in the azimuthal direction. Mode 5 has a more complex structure and does not correspond to a normal acoustic mode shape. Similar observations can be made for high swirl number S = 1.10. [39] All of these results indicate that the POD method is able to capture the detailed acoustic wave structure in the chamber. In fact, it is well established [40,41] that the optimal base functions obtained by the POD method consist of the Fourier modes in the homogeneous (periodic) coordinate directions, i.e., the azimuthal direction in the current case.

2.5.8 Energy Exchange Mechanism in Oscillatory Flowfield.

The instantaneous flowfield can be reconstructed from the POD modes by means of Eq. (5). Such a procedure allows us to examine how the various POD modes contribute to the instantaneous events occurring in the chamber. Figure 21 shows the time histories of the pressure and axial velocity, u_x, immediately downstream of the dump plane with $r = 15$ mm for S = 0.44. The reconstructed signals from the first two and first twelve modes are also included for comparison. The flowfield can be reasonably recovered with twelve modes and matches well the original data. The first two modes, however, can capture unambiguously the dominant flow motions in a complex turbulent flowfield through proper orthogonal decomposition. A similar observation were made for the high swirl number case with S = 1.10.

Figure 22 shows the temporal evolution of the reconstructed pressure and heat release field based on the first two POD modes on a transverse plane (x = 32 mm) over one cycle of the 1T mode of oscillation for two different swirl numbers. The spinning 1T acoustic wave motions in the azimuthal direction are clearly observed for both cases. The phenomenon can be mathematically attributed to the existence of two equal-valued eigenvalues corresponding to the 1T acoustic oscillation. According to Aubry et al. [42], the phenomenon is a result of the presence of traveling waves (or structures) in the flowfield, which is also related to the spatio-temporal symmetry of the system. The temporal evolution of the reconstructed heat-release field reveals the existence of helical structures in the shear-layer region during the flame development.

Since the acoustic (i.e. periodic) field is dominated by the 1T oscillation and can be well characterized by the first two POD modes, the entire fluctuating flowfield can be expressed as the sum of periodic and turbulent components as follows.

$$\hat{\mathbf{q}}'(\mathbf{x},t_m) = a^{(1)}(t_m)\boldsymbol{\varphi}^{(1)}(\mathbf{x}) + a^{(2)}(t_m)\boldsymbol{\varphi}^{(2)}(\mathbf{x}) + \sum_{n=3}^{M} a^{(n)}(t_m)\boldsymbol{\varphi}^{(n)}(\mathbf{x})$$

$$= \hat{\mathbf{q}}^a(\mathbf{x},t_m) + \hat{\mathbf{q}}^t(\mathbf{x},t_m)$$

(6)

This representation provides us with a convenient way to analyze the mechanisms of energy transfer among various constituent flowfields in the combustor. Figure 23 shows the distributions of $Ra = \overline{p^a \dot{q}^a}(\gamma - 1)/\overline{\gamma p}$, $R_{\rho uu} = \overline{\rho u_i^a u_j^a} \partial \overline{u}_i / \partial x_j$, and $R_{pu} = \overline{p^a \partial u_j^a / \partial x_j}$ for the 1T acoustic oscillation on a longitudinal and a transverse plane S = 0.44. Here the periodic components of fluctuating flowfield, p^a, $\dot{q}^a$ and u_i^a are obtained using above Equ. (6) through POD method. The Rayleigh parameter, Ra, represents the coupling between oscillatory heat release and pressure. It provides a qualitative measure of the extent to which unsteady heat release drives or suppresses flow oscillations. The acoustic motion is amplified if $Ra > 0$ or damped out if $Ra < 0$. For both swirl numbers, a wavy distribution of Ra takes place along the flame front. The Rayleigh parameter has a positive value in much of the flame zone. The 1T acoustic oscillation is favorably correlated with the unsteady heat release and extracts energy from chemical reactions. The parameter, $R_{\rho uu}$, characterizes the kinetic energy exchange between the mean and oscillatory flowfields. [39, 44] If $R_{\rho uu}$ is negative, energy is transferred from the mean to the oscillatory flowfield. A well organized distribution of $R_{\rho uu}$ is observed in the shear layers downstream of the backward-facing step and the center body. These structures, aligned with regions with alternate positive and negative values, exhibit strong interactions between the mean and periodic flowfields. The parameter, R_{pu}, stands for the exchange between the kinetic and potential energies of flow oscillations. [39, 44] Such an energy exchange process occurs almost everywhere in the chamber, but much more vigorously in regions of flame zone and central toroidal recirculation zone.

3. Three Dimensional Linear Acoustic Analysis of Combustion Instabilities

3.1 Model Description

   A reduced-order model is developed to determine the stability characteristics of the combustor [43,45], using LES results a basis. The analysis is capable of treating both longitudinal and transverse waves as well as their combinations in complex configurations with non-uniform distributions of mean flow properties. The basis of the analytical model is an integral approach, which can be established by integrating the conservation equations over a given cross section to obtain a system of ordinary differential equations. [3,4,43] By assuming linear harmonic motions in time, a wave equation governing flow oscillations is derived with expansion of the dependent variables in a small parameter measuring the amplitude of the unsteady motion. The wave equation can be written in a generic form:

$$\nabla^2 p^a - \frac{1}{\bar{a}^2}\frac{\partial^2 p^a}{\partial t^2} = h\left(\bar{u}, \bar{p}, u^a, p^a, \dot{Q}^a, \text{ etc.}\right) \tag{7}$$

subject to $\boldsymbol{n}\cdot\nabla p^a = -f$ along the boundary. The source terms h and f involve all the volumetric and surface effects. To account for spatial variations of the chamber geometry and mean flowfield, the combustor is discretized axially into a number of cells, as shown in Fig. 24, such that the mean axial flow properties within each cell can be taken to be uniform. Furthermore, the mean-flow Mach number on the transverse plane is assumed to be small, as in most practical combustion systems. The acoustic field in each cell is synthesized as a Fourier-type series in terms of the eigenfunctions for the cross section, but allows for temporal and axial variations through the series coefficients. In cylindrical coordinates, this can be expressed as

$$p^a(\boldsymbol{r},t) = \sum_{n=0}^{\infty}\sum_{m=-\infty}^{\infty}\left[\psi_{mn}(\theta,r)\eta_{mn}(x,t)\right] \tag{8}$$

The eigenfunction ψ_{mn} can be well approximated by that of a classical acoustic field without source terms. It satisfies the Helmholtz equation for the transverse plane and is subject to the homogeneous boundary condition along the combustor wall. The subscripts m and n stand for mode indices in the circumferential and radial directions, respectively. After expansion, a spatial-averaging technique is applied to solve for the axial variation of the acoustic field.

   The volumetric and boundary processes appearing on the right-hand side of the wave equation must be modeled. To facilitate formulation, the coefficients C_h and C_f are introduced to represent these terms, as shown below.

$$\iint \psi_{mn}\hat{h}\,ds = C_{h,mn}\hat{\eta}_{mn}(x)$$
$$\oint \psi_{mn}\hat{f}_T\,dl = C_{f,mn}\hat{\eta}_{mn}(x) \tag{9}$$

The source term arising from oscillatory combustion can be written as

$$h = -i\Omega\dot{Q}^a(\gamma-1)/\bar{a}^2 \tag{10}$$

Substituting Eq. (10) into Eq. (9), and applying the combustion response function derived in Ref. 45, the coefficient $C_{h,mn}$ is obtained as

$$C_{h,mn} = \iint \psi_{mn}G_{h,mn}\,ds \tag{11}$$

where

$$G_{hmn} = -\frac{i(\gamma-1)\Omega\bar{Q}\psi_{mn}}{\bar{a}^2}\cdot\left[\frac{R_p}{\bar{p}} - \frac{R_u}{\bar{\rho}\bar{u}(\Omega+\bar{u}\alpha_{mn})} - \frac{R_t m}{\bar{\rho}\bar{u}r(\Omega+\bar{u}\alpha_{mn})}\right] \tag{12}$$

After modeling the various source terms in the wave equation, the acoustic pressure field in each cell can be solved in the following form.

$$p^a(\boldsymbol{r},t) = e^{i\Omega t}\sum_{n=0}^{\infty}\sum_{m=-\infty}^{\infty}\left[\psi_{mn}(\theta,r)\hat{\eta}_{mn}(x)\right] \tag{13}$$

where

$$\hat{\eta}_{mn}(x) = p_{mn}^+\exp\left(i\alpha_{mn}^+x\right) + p_{mn}^-\exp\left(i\alpha_{mn}^-x\right) \tag{14}$$

The axial wave number α_{mn} is given by

$$\alpha_{mn}^2 = \left(\Omega^2/\bar{a}^2\right) - k_{mn}^2 - C_{h,mn} - C_{f,mn} \tag{15}$$

where Ω denotes the oscillation eigenfrequency, and k_{mn} is the eigenvalue corresponding to the transverse eigenfunction ψ_{mn}.

   The oscillatory flow properties in each cell are matched with those in the adjacent cells at the cell interfaces by enforcing the conservation laws. The procedure eventually leads to a system equation which determines the stability characteristics and spatial structure of the acoustic waves in the entire system. The resultant characteristic frequency Ω is complex.

$$\Omega = \Omega_r + i\Omega_i \tag{16}$$

The real part Ω_r is the radian frequency, and the imaginary part Ω_i is referred to as the damping coefficient because its value determines the decay rate of a particular acoustic mode. Compared with conventional numerical methods, the present analysis is compact and efficient, and can be effectively used to investigate gas-turbine combustion instability.

3.2 Application to a Lean-Premixed Combustor

As a specific example, we consider the lean-premixed swirl-stabilized combustor described in the preceding section, as shown in Fig. 1. Based on the experimental and numerical results, two cases are investigated in the present study. Case 1 is associated with a stable operating condition with an inlet temperature of 600 K, and Case 2 corresponds to an unstable situation with an inlet temperature of 660 K. The average flame-spreading angles are estimated from the calculated mean-temperature fields. These quantities along with the mean-flow properties are used to determine the combustion response function, [45] which is then employed in the generalized acoustic analysis to characterize the stability behavior of the combustor. Table 2 summarizes the calculated oscillation frequencies and damping coefficients of the first longitudinal (1L), first tangential (1T), and first radial (1R) modes for both cases. The results agree well with the experimental observations (Broda et al. 1998) and LES calculations. For the enveloped flame (Case 2), the calculated frequency of 1753 Hz matches closely the experimental value of 1750 Hz. The spatial distribution of the first longitudinal mode shown in Fig. 25 also demonstrates the validity of the present analysis.

4. Intelligent Control of Gas Turbine Combustion Dynamics

An integrated control methodology has been established for gas-turbine engine combustors in order to improve performance in terms of lean blowout and combustion stability characteristics, and to reduce pollutant emissions. The work covers all three aspects of gas dynamics, combustion, and control synthesis involved in constructing an intelligent gas-turbine combustor. A variety of active control techniques are systematically evaluated and implemented in a hierarchical approach. [46,47,48,49] Both steady-state and transient operations relevant to practical engine working conditions are faithfully treated. In addition, innovative concepts for diagnostic and prognostic decision-making are incorporated into the control system to enhance engine reliability, availability, and maintainability. Optimization of combustor operations is conducted based on requirements for flame stability and pollutant emissions.

The combustor control system consists of two interacting modules: *slow-time supervisory* controller and *fast-time flame* controller, as shown in Fig. 26. [48] The *slow-time supervisory* controller in the outer loop is synthesized with robust linear control techniques that rely on low-order dynamics models in the state-variable setting. The *fast-time flame* controller in the inner loop is responsible for suppression of combustion instabilities and for prevention of the lean blowout of the flame. The control strategy previously developed by Hong et al. [47] in a deterministic setting with constant transport delays is extended to accommodate model uncertainties, plant disturbances, and sensor noises. In addition, novel nonlinear stochastic control methodologies are employed to compensate the random time delays associated with distributed combustion processes. Emphasis is placed on the controller robustness and efficiency.

The wide-range control of combustion dynamics is realized as an L_2-gain linear parameter-varying (LPV) system that has been synthesized in the setting of differential game theory. The output feedback control of fast-time-scale variables is gain-scheduled as C^1-continuous functions of slow-time-scale parameters. The salient features of the proposed LPV L_2-gain control are: (i) no explicit dependence on the temporal rates of the gain-scheduling variables; and (ii) structural similarity with the finite-dimensional linear time-invariant (FDLTI) H_∞ control law of Doyle-Glover-Khargonekar-Francis.

The robustness of the LPV control law has been evaluated under wide range operation of a generic combustor where the effects of modeling uncertainties are included in the design. The plant under consideration is representative of a generic model for several types of air-breathing combustors, such as the model combustor shown in Fig. 1, and those used in ramjet and gas-turbine engines. Fuel and oxidizer are delivered to the combustion chamber, in which large excursions of unsteady motions take place due to the internal coupling between flow oscillations and transient response of combustion. The strategy, originally proposed by Fung *et al.*, [46] is followed for robust closed-loop control of combustion instabilities by Hong *et al.* [47,48] First, the instantaneous chamber conditions are monitored by sensors at sufficiently high sampling rates to capture the transient characteristics of unsteady motions. The sensor signals are then processed by a controller to modulate the mass flow rate of a secondary supply of fuel. The injected fuel reacts with the combustor flow as it travels downstream, exerting a distribution of external influences on the oscillatory flowfield for instability control.

The control of the acoustic dynamics in the combustion chamber is realized by making a trade-off between the amplitude of pressure oscillation and the secondary fuel injection rate. The control laws are synthesized based on a multiple-time-scale model of combustion dynamics. Control actions of secondary fuel injection on

the fast-time scale are gain-scheduled according to the variations of the mean gas velocity and temperature on the slow-time scale. The LPV control law is synthesized with due consideration to temporal variation rates in the scheduling variables: the mean gas velocity and temperature. Pertinent results of the simulation experiments are presented in Figs. 27 and 28. [48]

Figure 27 shows the temporal trajectories of the scheduling variables, i.e., mean gas velocity and temperature, that are normalized over the full range. Figure 28 show the responses of the first two modes of pressure oscillations in the chamber under the LPV robust control. The observer embedded in the LPV robust controller is capable of estimating acoustic vibration of each mode under a wide range of continuously varying scheduling parameters.

5. Conclusions

Both numerical simulation and analytical modeling have been conducted to study the combustion dynamics in lean-premixed (LPM) swirl-stabilized combustors. The numerical analysis is based on a large-eddy simulation technique along with a level-set flamelet library approach. Emphasis is placed on the key mechanisms and operation parameters responsible for driving combustion oscillations. The results indicated that the inlet air temperature and equivalence ratio are the key parameters determining the stability characteristics of the combustor. A slight increase in the inlet flow temperature across the stability boundary leads to a transition from a stable to an unstable flame and consequently results in a sudden increase in acoustic flow oscillation. For an oscillatory flame, the thermal energy released from chemical reactions in the flame zone is fed to acoustic fluctuations in the chamber through a closed-loop feedback process, which includes the mutual coupling between acoustics excitation, vortex shedding, flame motion, and heat-release oscillation. Much information has been obtained to shed light to the fundamental mechanisms for initiating and sustaining combustion instabilities in gas-turbine engines. A companion reduced-order model based on a generalized wave equation is also established to facilitate data analysis and to help transfer the LES results to a form that can be effectively used to predict the combustion stability characteristics of a full-scale gas turbine engine. The analytical model also serves as backbone for devising control techniques to modulate combustion processes.

REFERENCES

1. Correa, S.M. "A Review of NO_X Formation under Gas-turbine Combustion Conditions", *Combustion Science and Technology,* Vol.87, 1993, pp.329-362.
2. Lefebvre, A. H. "The Role of Fuel Preparation in Low-emission Combustion", ASME *Journal of Engineering for Gas Turbines and Power,* Vol.117, 1995, pp.617-654.
3. Culick, F.E.C., and Yang, V., "Prediction of the Stability of Unsteady Motions in Solid Propellant Rocket Motors," Chapter 18, *Nonsteady Burning and Combustion Stability of Solid Propellants*, Progress in Astronautics and Aeronautics, Vol. 143, eds., L. DeLuca and M. Summerfield, 1992, pp. 719-779.
4. Culick, F.E.C., and Yang, V., "Overview of Combustion Instabilities in Liquid-Propellant Rocket Engines," Chapter 1, *Liquid Rocket Engine Combustion Instability*, Progress in Astronautics and Aeronautics, Vol. 169, eds., V. Yang and W. E. Anderson, 1995, pp. 3-37.
5. Knoop, P., Culick, F.E.C., and Zukoski, E.E., "Extension of the Stability of Motions in a Combustion Chamber by Nonlinear Active Control Based on Hysteresis," *Combustion Science and Technology*, Vol.123, 1997, pp.263-376.
6. Broda, J.C., Seo, S., Santoro, R.J., Shirhattikar, G. and Yang, V., "An Experimental Study of Combustion Dynamics of a Premixed Swirl Injector", *Proceedings of the Combustion Institute*, Vol.27, 1998, pp.1849-1856.
7. Lieuwen, T., "Experimental Investigation of Limit-Cycle Oscillations in an Unstable Gas-Turbine Combustor," *Journal of Propulsion and Power*, Vol.18, 2003, pp.61-67.
8. Huang, Y., Sung, H.G., Hsieh, S.Y. and Yang, V., "Large Eddy Simulation of Combustion Dynamics of Lean-Premixed Swirl-Stabilized Combustor," *Journal of Propulsion and Power*, Vol.19, 2003, pp.782-794.
9. Poinsot, T.J., Trouve, A.C., Veynante, D.P., Candel, S., and Esposito, E., "Vortex-driven Acoustically Coupled Combustion Instabilities," *Journal of Fluid Mechanics*, Vol.177, 1987, pp.165-292.
10. Schadow, K.C. and Gutmark, E., "Combustion Instability Related to Vortex Shedding in Dump Combustor and Their Passive Control", *Progress in Energy and Combustion Science*, Vol.18, 1992, pp.117-132.
11. Lieuwen, T. and Zinn, B.T. "The Role of Equivalence Ratio Oscillation in Driving Combustion Instabilities in Low Nox Gas Turbines", *Proceedings of the Combustion Institute*, Vol. 27, 1998, pp.1809-1816.
12. Venkataraman, K.K., Preston, L.H., Simons, D.W., Lee, B.J., Lee, J.G., and Santavicca, D.A., "Mechanism of Combustion Instability in a Lean Premixed Dump Combustor," *Journal of Propulsion and Power*, Vol.15, 1999, No.6, pp 1999.
13. Huang, Y., and Yang, V., "Bifurcation of Flame Structure in a Lean-Premixed Swirl-Stabilized Combustor: Transition from Stable to Unstable Flame," *Combustion and Flame*, Vol. 136, 2004, pp. 383-389.
14. Huang, Y., and Yang, V., "Effect of Swirl on Combustion Dynamics in a Lean-Premixed Swirl-Stabilized Combustor," *Proceedings of the Combustion Institute*, Vol. 30, 2004, pp. 1771-1778.
15. Johnson, C.E., Neumeier, Y., Lieuwen, T.C. and Zinn, B.T., "Experimental Determination of the Stability Margin of A Combustor Using Exhaust Flow and Fuel Injection Rate Modulations," *Proceeding of Combustion Institute,* Vol. 28, 2000, pp.757-763.

16. Lee, S.Y., Seo, S., Broda, J.C., Pal, S. and Santoro R.J., "An Experimental Estimation of Mean Reaction Rate and Flame Structure During Combustion Instability in a Lean Premixed Gas Turbine Combustor," *Proceeding of Combustion Institute,* The Combustion Institute. Vol. 28, 2000, pp.775-782.

17. Seo, S., "Parametric Study of Lean Premixed Combustion Instability in a Pressured Model Gas Turbine Combostor," *Ph.D. Thesis*, Department of Mechanical Engineering, The Pennsylvania State University. University Park, PA, 1999.

18. Erlebacher, G., Hussaini, M.Y., Speziale, C.G. and Zang, T.A., "Toward the Large Eddy Simulation of Compressible Turbulent Flows", *Journal of Fluid Mechanics*, Vol.238, 1992, pp.155-158

19. Poinsot, T. and Lele S., "Boundary Conditions for Direct Simulation of Compressible viscous flows", *Journal of Computational Physics*, Vol.101, 1992, pp.104-129

20. Swanson, R.C. and Turkel, E., "On Central-difference and Upwind Schemes", *Journal of Computational Physics*, Vol.101, 1992, pp.292-306

21. Oefelein, J.C. and Yang, V., "Modeling High-Pressure Mixing and Combustion Processes in Liquid Rocket Engines", *Journal of Propulsion and Power,* Vol.14, 1998, pp.843-857

22. Apte, S., and Yang, V., "Unsteady Flow Evolution and Combustion Dynamics of Homogeneous Solid Propellant in a Rocket Motor," *Combustion and Flame*, Vol. 131, 2002, pp. 110-131.

23. Rayleigh, J.W.S., 1945, *The Theory of Sound*, Vol. II, Dover, New York.

24. Lewis, B. and von Elbe, G., *Combustion, Flames and Explosions of Gases*, 3rd ed. Academic press, New York, pp.233-236 (1987)

25. Kurdyumov, V.N., Fernandez, E. and Linan, A., "Flame Flashback and Propagation of Premixed Flames near a Wall," *Proceeding of Combustion Institute*, Vol.28, pp.1883-1889, 2000.

26. Thibaut, D. and Candel, S., "Numerical Study of Unsteady Turbulent Premixed Combustion: Application to Flashback Simulation," *Combustion and Flame,* Vol.113, 1998, pp.53-65.

27. Najm, H.N. and Ghoniem, A.F., "Coupling Between Vorticity and Pressure Oscillations in Combustion Instability," *Journal of Propulsion and Power*, Vol.10, pp.769-776, 1994

28. Lieuwen, T., Torres,H., Johnson,C. and Zinn,B.T., "A Mechanism of Combustion Instability in Lean-Premixed Gas-Turbine Combustor," *Journal of Engineering for Gas and Turbine and Power*, 123:182-189(2001)

29. Lipatnikov, A.N. and Chomiak, J., "Turbulent Flame Speed and Thickness: Phenomenology, Evaluation and Application in Multi-dimensional Simulations," *Progress in Energy and Combustion Science*, Vol.28, pp.1-74, 2000

30. Chao, Y.C., Leu, J.H. and Huang, Y.F., "Downstream Boundary Effects on the Spectral Characteristics of a Swirling Flowfield," *Experiments in Fluids*, Vol.10, 1991, pp.341-348.

31. Liu, T., Huang, Y., and Yang, V., "Linear Stability Analysis of Annular Swirling Jets," to be submitted to *Physical of Fluids*, 2005.

32. Peng, D., Merriman, B., Osher, S., Zhao. H., and Kang, M., "A PDE-Based Fast Local Level-Set Method, *Journal of Computational Physics*, Vol. 155, 1999, pp.410-438.

33. Fedkiw, R.P., Sapiro, G. and Shu, C.W., "Shock Capturing, Level Sets, and PDE based Methods in Computer Vision an Image Processing: a Review Of Osher's Contributions," *Journal of Computational Physics*, Vol.185, 2003, pp.309-341.

34. Sirvoich, L., Kirby, M. and Winter, M., "An Eigen-Function Approach to Large Scale Transitional Structures in Jet Flow," *Physics of Fluids*, Vol. 2(2), 1992, pp.127-136.

35. Sirovich, L., "Turbulence and the Dynamics of Coherent Structures, Part 1: Coherent Structures, *Quarterly of Applied Mathematics*, Vol. 45(3), 1987, pp.561-571.

36. Rowley, C.W., Colonius, T. and Murray, R.M., "Model Reduction for Compressible Flows Using POD and Galerkin Projection," *Physica D.* Vol.189, 2004, pp.115-129.

37. Berkooz, G., Holmes, P. and Lumley, J.L., "The Proper Orthogonal Decomposition in the Analysis of Turbulent Flows," *Annual Review of Fluid Mechanics*, Vol. 25, 1993, pp.539-575.

38. Cordier, L. and Bergmann, M., "Proper Orthogonal Decomposition: an Overview," *Post-Processing of Experimental and Numerical Data*, von Karman Institute for Fluid Dynamics, Lecture Series 2003-03, 2003.

39. Huang, Y., Wang, S., and Yang, V., "A Systematic Analysis of Combustion Dynamics in a Lean-Premixed Swirl-Stabilized Combustor*," AIAA Journal* (Submitted), 2005.

40. George, W.K., "Insight into the Dynamics of Coherent Structures from a Proper Orthogonal Decomposition." *Symposium on Near Wall Turbulence*, Dubrovnik, Yugoslavia. 1988.

41. Holmes, P., Lumley, J.L. and Berkooz, G., *Turbulence, Coherent Structures, Dynamical Systems and Symmetry*, Cambridge University Press, Cambridge, 1996.

42. Aubry, N., Guyonnet, R. and Lima, R., "Spatio-Temporal Symmetries and Bifurcation via Bi-Orthogonal Decompositions," *Journal of Nonlinear Science*, Vol. 2, 1992, pp.183-215.

43. You, D.-N., Sun X.-F., and Yang, V., "A Generalized Linear Theory of Three-Dimensional Combustion Instability," submitted to *Journal of Fluid Mechanics*, 2004.

44. Huang, Y., "Modeling and Simulation of Combustion Dynamics in Lean-Premixed Swirl-Stabilized Gas-Turbine Engines," Ph.D. Dissertation, Department of Mechanical Engineering, The Pennsylvania State University, University Park, PA, 2003.

45. You, D., Huang, Y., and Yang, V., "A Generalized Model of Acoustic Response of Turbulent Premixed Flame and Its Application to Gas-Turbine Combustion Instability Analysis," *Combustion Science and Technology* (accepted for publication), 2005.

46. Fung, Y.T., Yang, V. and Sinha, A., "Active Control of Combustion Instabilities Distributed Actuators," *Combustion Science and Technology*, Vol. 78, 1991, pp. 217-245.

47. Hong, B.S., Yang, V., and Ray, A., "Robust Feedback Control of Combustion Instability with Modeling Uncertainty," *Combustion and Flame*, Vol. 120, 2000, pp. 91-106.

48. Hong, B.S., Ray, A., and Yang, V., "Wide-Range Robust Control of Combustion Instability," *Combustion and Flame*, Vol. 128, 2002, pp. 242-258.

49. Hong, B.S., Ray, A., and Yang, V., "Output Feedback Linear Parameter Varying (LPV) L_2-Gain Control," *ASME Journal of Dynamics Systems, Measurement, and Control*, Vol. 125, 2003, pp. 485-489.

Table 1 Oscillation Frequencies Predicted by Linear Acoustic Modal Analysis

Mode	Frequency, Hz
First Longitudinal (1L)	1,760
First Tangential (1T)	10,712
Second Tangential (2T)	17, 820
First Radial (1R)	22,456

Table 2 Calculated oscillation frequencies and damping coefficients for a swirl-stabilized combustor

Mode	Case 1 (T_{in} = 660 K)		Case 2 (T_{in} = 660 K)	
	Frequency (Hz)	Damping coefficient (s^{-1})	Frequency (Hz)	Damping coefficient (s^{-1})
1L	1,645	2.1	1,753	−21
1T	10,610	0.9	11,310	−3.3
1R	22,297	3.5	24,236	−4.5
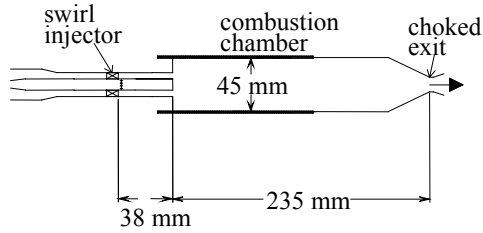
Fig. 1 Schematic of a model swirl-stabilized combustor (Broda, et al., 1998)
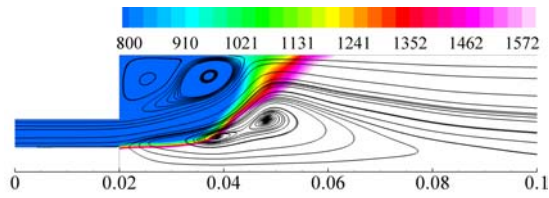
Fig. 2 Mean temperature contours and streamlines of stable flame for S = 0.76.
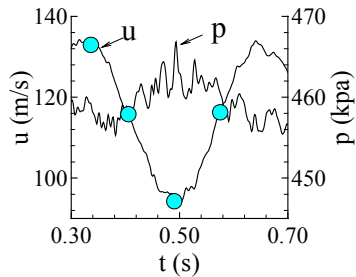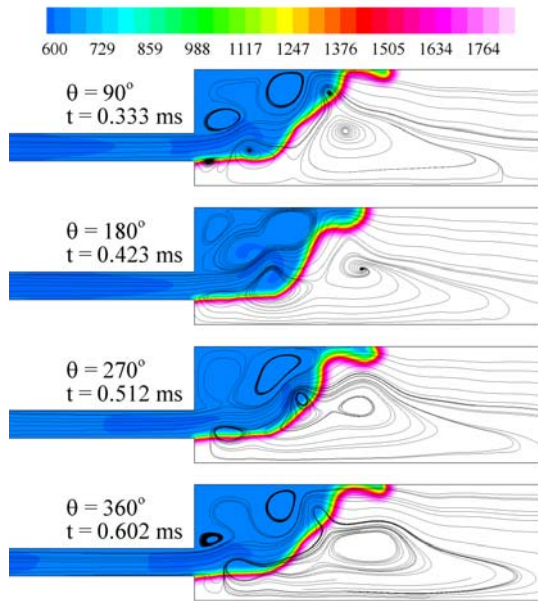
Fig. 3 Stable flame evolution over one cycle of oscillation (3214*Hz*): temperature contours and streamlines for S = 0.76.
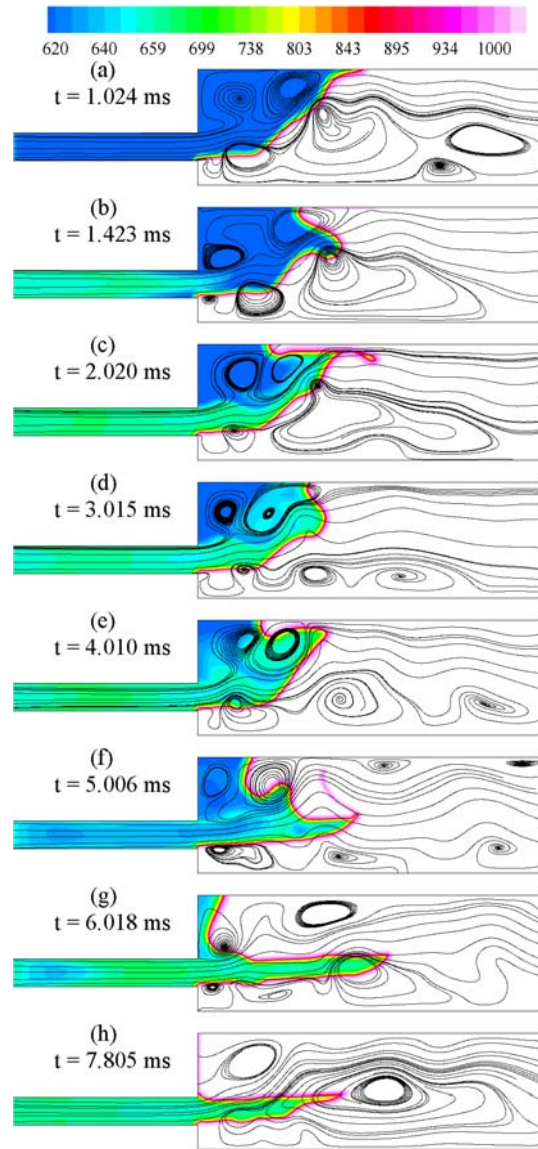
Fig. 4 Transition from stable to unstable flame with increased inlet temperature from 600 to 660 K for S = 0.76.
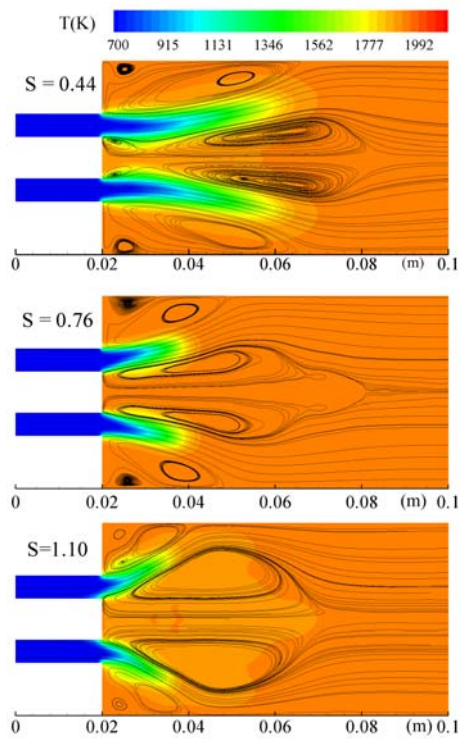
Fig. 5 Mean temperature fields and streamline patterns for S = 0.44, 0.76 and 1.10.
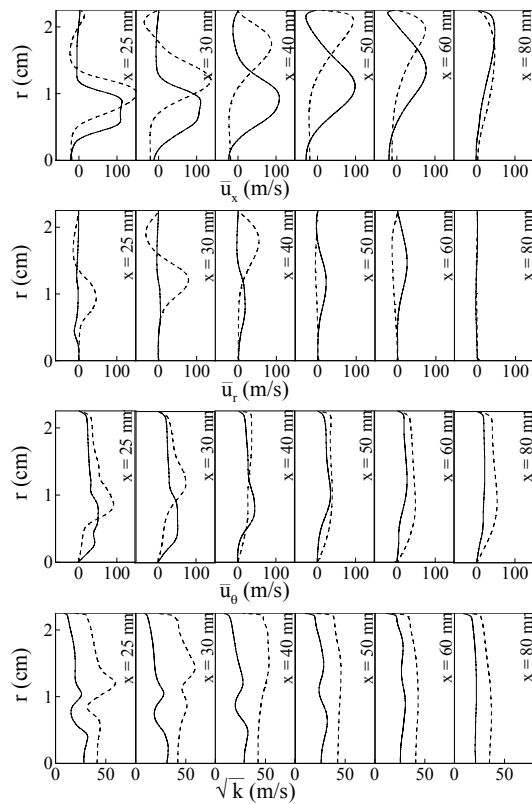
Fig. 6 Radial distributions of mean velocity components and turbulent kinetic energy at various axial locations for S = 0.44 and 1.10.
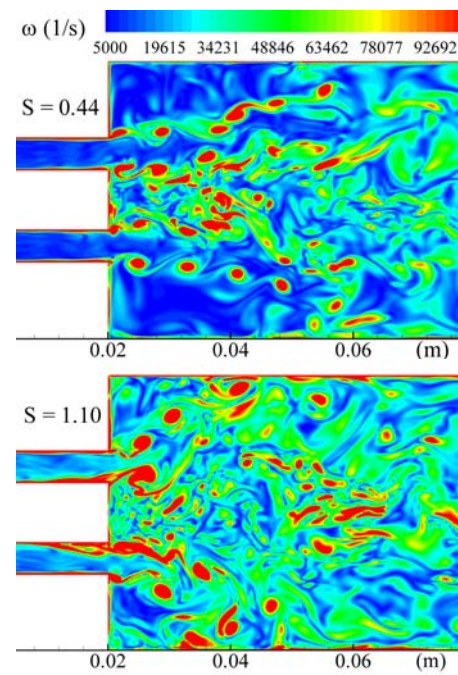
Fig. 7 Snapshots of vorticity magnitude field on an $x - r$ plane for S = 0.44 and 1.10.
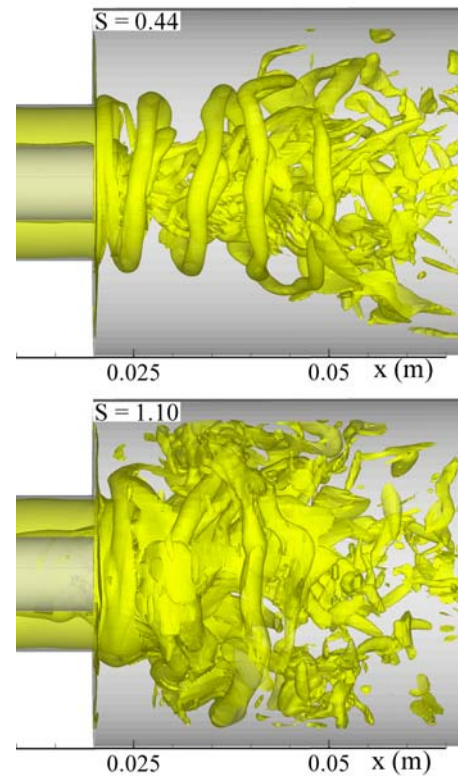
Fig. 8 Snapshots of iso-vorticity surface at ω =75000 s^{-1} ($r > 0.02$ m is blanked) for S = 0.44 and 1.10.
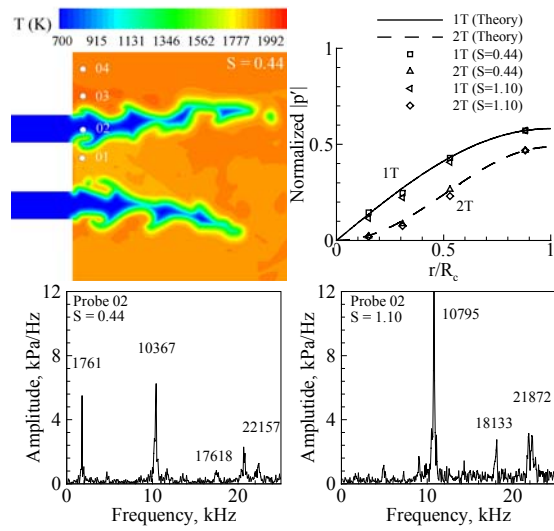
Fig. 9 Power spectral densities of pressure fluctuations immediately downstream of the dump plane and spatial distributions of 1T and 2T modes of acoustic oscillations for S = 0.44 and 1.10.
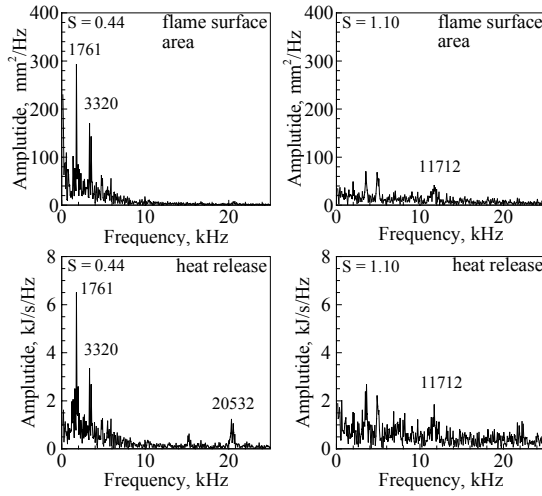
Fig. 10 Power spectral densities of total flame-surface area and heat-release fluctuations for S = 0.44 and 1.10.
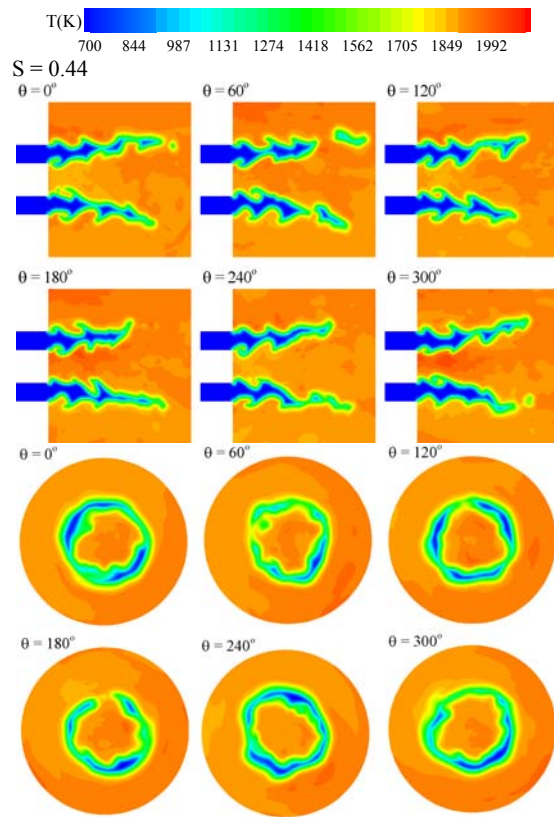
Fig. 11 Temporal evolution of temperature field over one cycle of 1L mode of oscillation for S = 0.44.
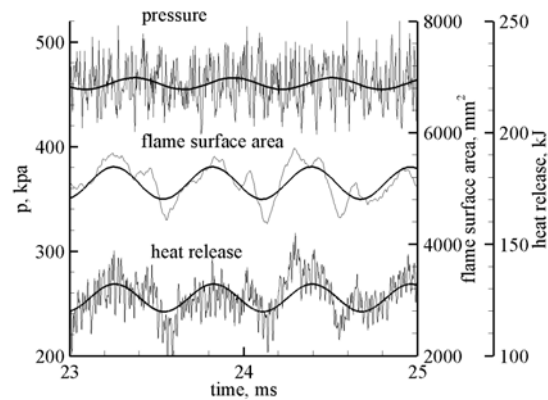
Fig. 12 Time histories of pressure immediately downstream of dump plane (top), heat release rate (middle), and flame surface-area (bottom) for S = 0.44, thick black lines represent the extracted 1L oscillations.
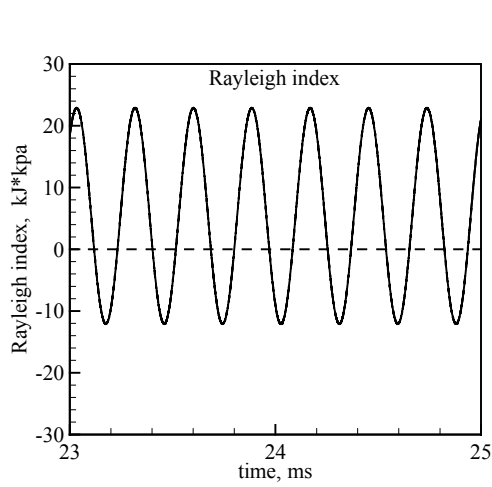
Fig. 13 Time evolution of ($p^a \cdot \dot{Q}^a(t)$) over entire chamber for 1L mode of oscillation for S = 0.44.
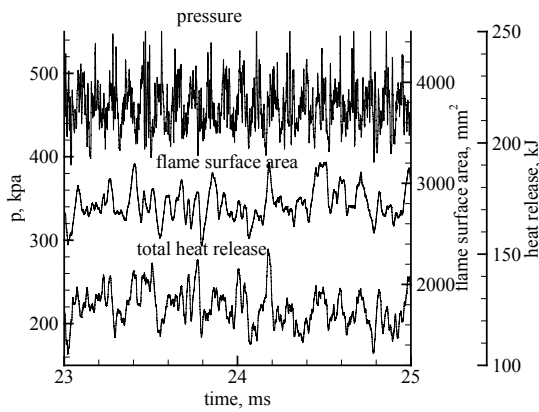
Fig. 14 Time histories of pressure immediately downstream of dump plane (top), flame surface-area (middle), and heat release rate (bottom) for S = 1.10.
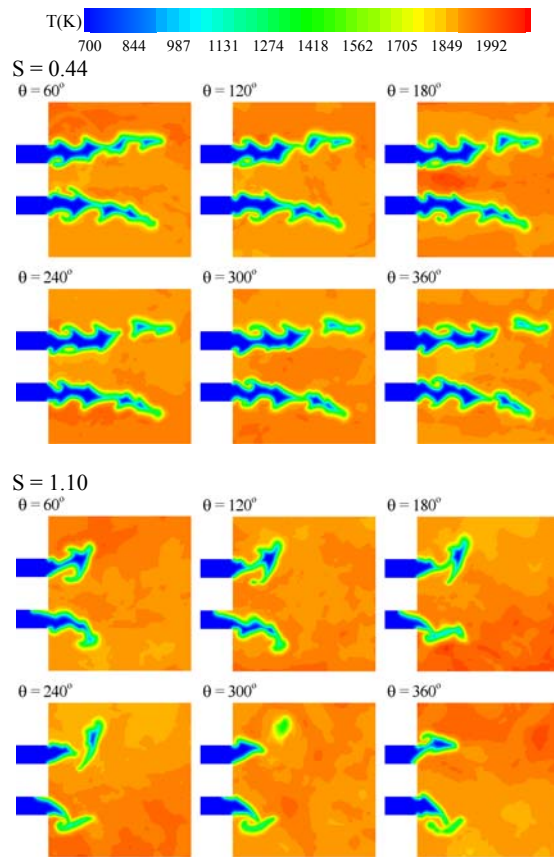
Fig. 15 Temporal evolution of temperature field over one cycle of 1T mode of oscillation for two different swirl numbers.
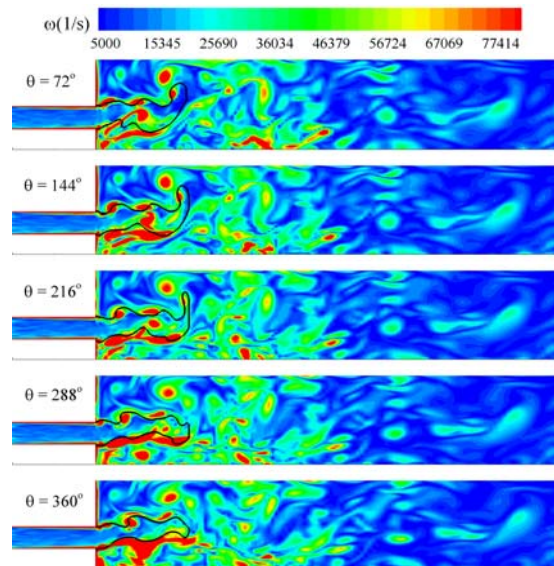
Fig. 16 Vortex and flame front interaction over one cycle of 1T mode of oscillation for S=0.76.

vorticity surface   flame surface   heat release
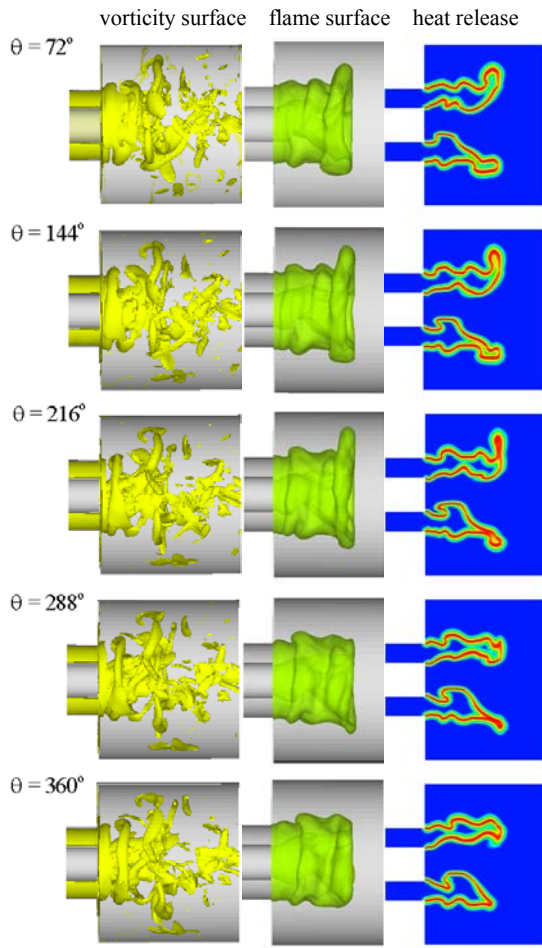
Fig. 17 Iso-vorticity surface of ω =75000 s^{-1} ($R>0.02m$ is blanked), iso-thermal surface of T=1700K, and normalized heat release contour over one cycle of first tangential mode of oscillation.
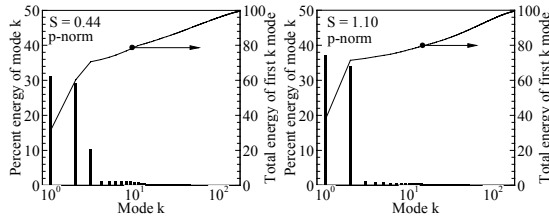
Fig. 18 Energy distributions of POD modes based on acoustic pressure fields for S = 0.44 and 1.10.
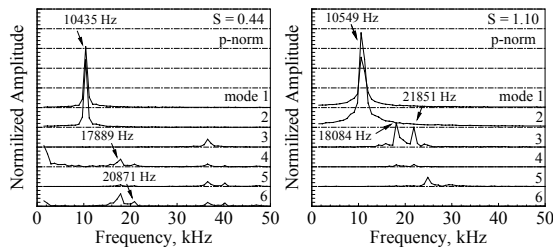
Fig. 19 Frequency spectra of time-varying coefficients of first six POD modes based on acoustic pressure fields for S = 0.44 and 1.10.
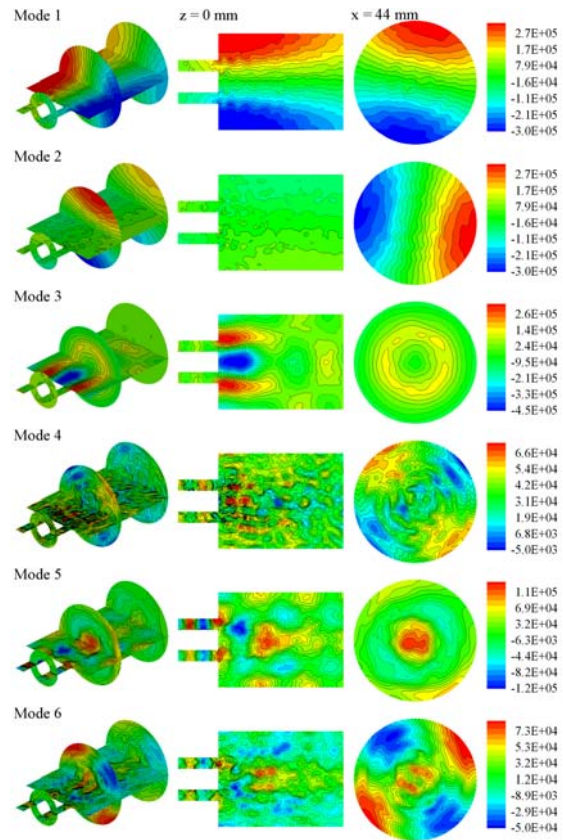
Fig. 20 Spatial distributions of first six POD modes of pressure field for S = 0.44.
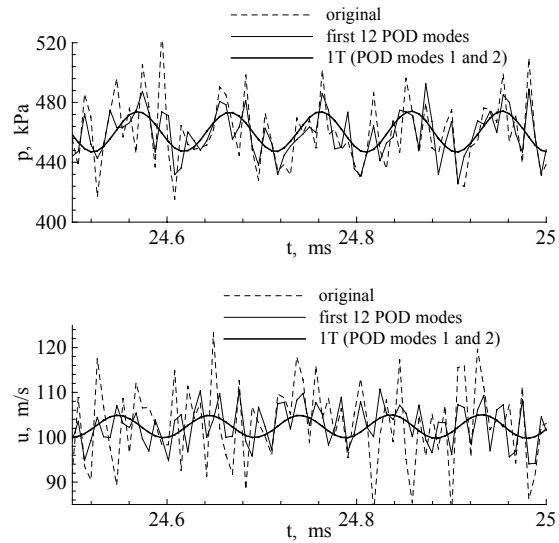
Fig. 21 Time histories pressure and axial velocity immediately downstream of dump plane for S = 0.44

Huang and Yang   19

a)

b)
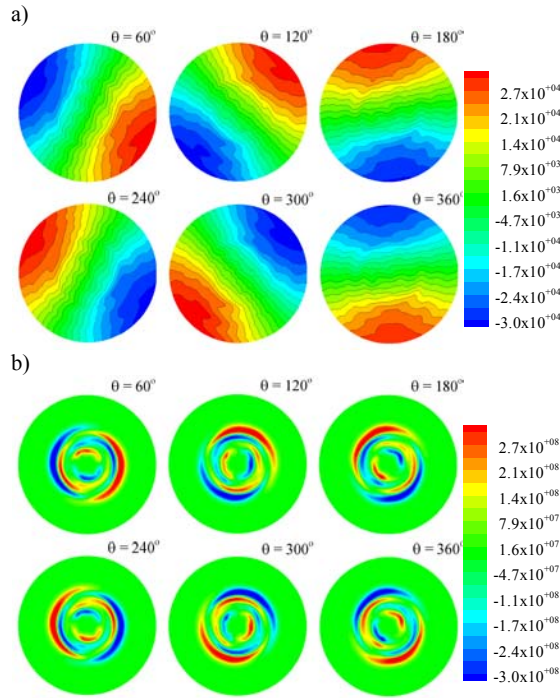
Fig .22 Temporal evolution of pressure (a) and heat release (b) field reconstructed based on first two POD modes on a transverse plane (x = 32 *mm*) over one cycle of 1T mode of oscillation for S = 0.44.
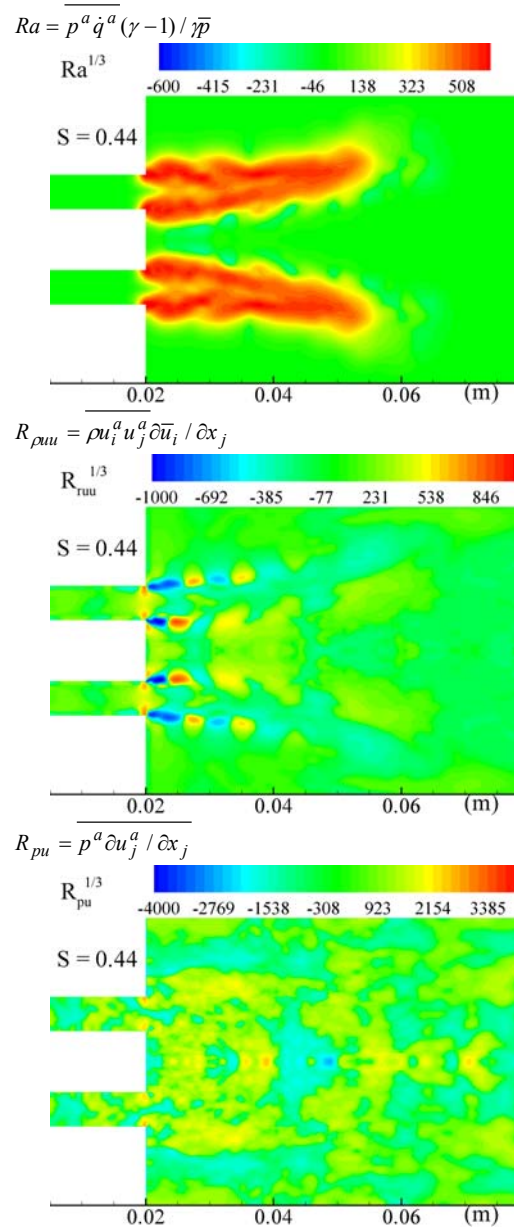
$$Ra = \overline{p^a \dot{q}^a}(\gamma - 1)/\gamma\overline{p}$$

$$R_{\rho uu} = \overline{\rho u_i^a u_j^a}\, \partial \overline{u}_i / \partial x_j$$

$$R_{pu} = \overline{p^a \partial u_j^a / \partial x_j}$$

Fig. 23 Distributions of $Ra = \overline{p^a \dot{q}^a}(\gamma - 1)/\gamma\overline{p}$,

$R_{\rho uu} = \overline{\rho u_i^a u_j^a}\, \partial \overline{u}_i / \partial x_j$, and $R_{pu} = \overline{p^a \partial u_j^a / \partial x_j}$ for 1T

oscillations on $x - r$ and $r - \theta$ planes at S = 0.44.
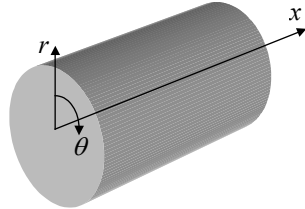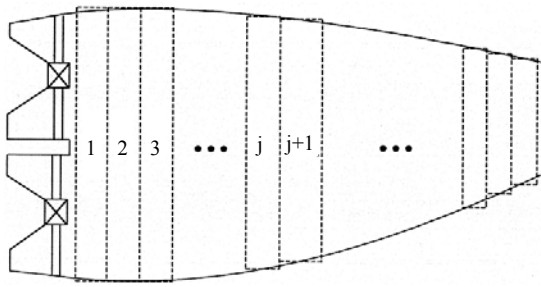
Fig. 24 Discretization of combustion chamber into cells in axial direction.
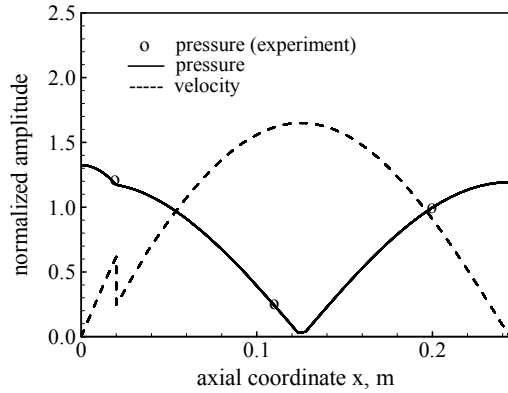

Fig. 25 Distributions of acoustic oscillations in swirl-stabilized combustor, first longitudinal mode.
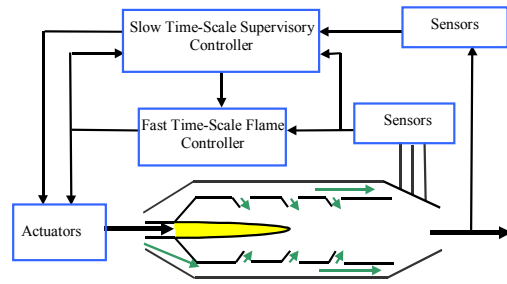

Fig. 26 Two layer control system for manipulating combustion dynamics.
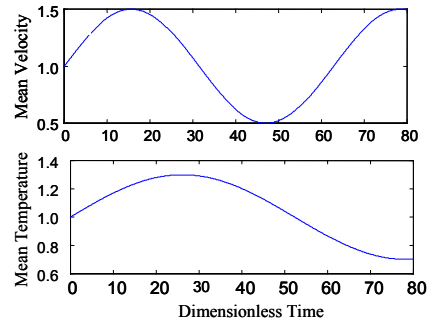

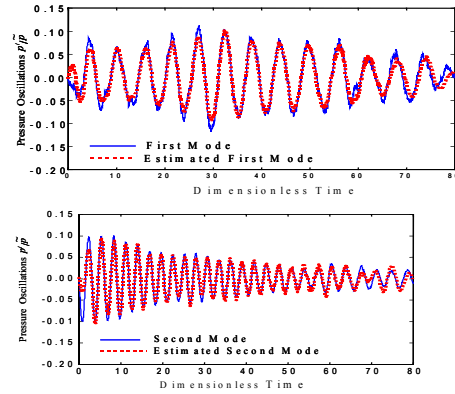
Fig. 27 Normalized mean velocity and mean temperature.

Fig. 28 Pressure oscillations of the first and second modes.